Nano Research

Open Access

Research Article

Oriented nanoconfined β-crystals enhance mechanical properties in regenerated silk fibroin nanocomposites

Hangsheng Zhou[1,2,4,§], Yunfei Ru[1,2,§], Hao Fu[2], Hao Zha[2], Can Zhou[2], Linxing Liu[2], Chuangqi Zhao[5,6], Jin Huang[1,2] ✉, and Mingjie Liu[1,2,3] ✉

[1] *State Key Laboratory of Bioinspired Interfacial Materials Science, Bioinspired Science Innovation Center, Hangzhou International Innovation Institute, Beihang University, Hangzhou 311115, China*
[2] *Key Laboratory of Bioinspired Smart Interfacial Science and Technology of Ministry of Education, School of Chemistry, Beihang University, Beijing 100191, China*
[3] *International Research Institute for Multidisciplinary Science, Beihang University, Beijing 100191, China*
[4] *State Key Laboratory of Spintronics, Hangzhou International Innovation Institute, Beihang University, Hangzhou 311115, China*
[5] *State Key Laboratory of Bioinspired Interfacial Materials Science, School of Chemistry and Materials Science, University of Science and Technology of China, Hefei 230026, China*
[6] *State Key Laboratory of Bioinspired Interfacial Materials Science, Suzhou Institute for Advanced Research, University of Science and Technology of China, Suzhou 215123, China*
§ *Hangsheng Zhou and Yunfei Ru contributed equally to this work.*

Cite this article: *Nano Research*, **2026**, *19*, 94908475. https://doi.org/10.26599/NR.2026.94908475

ABSTRACT: To tackle the severe plastic pollution, degradable materials with excellent mechanical properties are urgently needed. Silk protein materials with abundant sources, low cost, and good biocompatibility can be ideal candidates. However, due to the destruction of the original hierarchical structure of natural silk during processing, the mechanical properties of regenerated silk are usually significantly reduced. Here, we report a general strategy for constructing regenerated silk fibroin composites with high mechanical properties by introducing oriented nanoconfined β-crystals. Specifically, regenerated silk was introduced into the two-dimensional nanoconfined space of montmorillonite nanosheets, and an alcohol reagent was used to induce its secondary structure to transform from random coils/α-helices/β-turns to β-sheets, further forming β-crystals. These materials exhibit excellent mechanical properties with a tensile strength of 452.31 ± 21.23 MPa and modulus of 21.67 ± 0.24 GPa, superior to most plastics and polymer nanocomposites. In addition, these materials are biodegradable and can be fabricated in large areas.

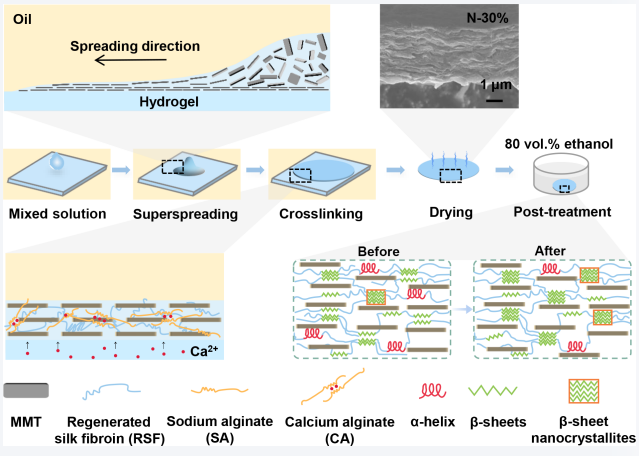

KEYWORDS: regenerated silk composites, high mechanical properties, oriented nanoconfined β-crystals, degradable, oriented structure

1 Introduction

In recent years, the environmental problems caused by plastic pollution have attracted considerable attention [1]. Plastics go through a linear cycle from fossil fuels to landfills, causing serious environmental pollution and ecological damage [2]. Therefore, there is an urgent need to find sustainable alternatives to synthetic plastics. The development of biodegradable products from renewable resources, such as natural biopolymers, is the best option [3]. Among the many natural materials, silk has always been of great interest due to its excellent mechanical properties and the maturity of its industrial production [4].

Silk is a natural fiber with a hierarchical structure, consisting of silk fibroin (SF) and its wrapped sericin protein [5], which contains

Received: November 27, 2025; **Revised:** January 7, 2026
Accepted: January 21, 2026

✉Address correspondence to Jin Huang, huangjin2018@buaa.edu.cn; Mingjie Liu, liumj@buaa.edu.cn

eighteen types of amino acids. Various amino acids can form a variety of secondary structures through hydrogen bond interaction, such as α-helix, β-sheet, random coil, etc. [6]. In addition, β-sheets can form β-crystal networks, in which β-crystals are interconnected through the amorphous chains (α-helix and/or random coil). The semicrystalline structure contributes to the strength, which plays a key role in the mechanical properties of silk protein [7]. Natural silk fiber has a modulus of 5–12 GPa, tensile strength of 400 MPa, and tensile elongation at break of approximately about 22% [5]. In order to process fiber biopolymers into materials suitable for the target application, silk fibrin extracted from the silkworm cocoon is typically regenerated by degumming, dissolution, and dialysis [8–11]. Regenerated silk solution allows silk fibroin to be processed in the form of an aqueous solution, resulting in a variety of material forms, such as films, electrospun fibers, gels, etc. [12]. However, these regenerated silk materials have a significant reduction in mechanical properties compared to natural silk due to the destruction of the original hierarchical structure of natural silk during processing.

In recent years, many empirical strategies have been tried to improve the mechanical properties of regenerated silk materials by adding nanofillers, annealing, solvent treatment, and crosslinking [13–17]. Tsukruk and co-workers prepared layered nanocomposites of graphene oxides (GO) and regenerated silk fibroin (RSF) using a layer-by-layer self-assembly method [18]. They also used water steam annealing to enable the assembly of silk fibroin near the GO surface into nanofibrils. These materials exhibit high tensile strength and toughness, reaching ~ 460 MPa and ~ 2.1 MJ/m^3, respectively. In addition, alcohol reagents contain a large number of hydroxyl groups, which can also break the hydrogen bonds formed between the original amino acids in silk fibroin, thus inducing their secondary structure transitions [19]. Enzyme pre-crosslinked regenerated silk fibroin hydrogels were post-treated with ethanol solution, and their strength and Young's modulus increased from 0.14 ± 0.02 to 0.70 ± 0.12 MPa and from 0.26 ± 0.04 to 2.51 ± 0.10 MPa, respectively [20]. To improve the toughness of RSF, a crosslinked network can be introduced to enhance its elongation at break. In physical crosslinking, silk fibroin molecules are linked by non-covalent bonds, which can induce the silk fibroin molecules to change from a random coil structure to a β-folded conformation [21]. In contrast, chemical crosslinking is the construction of stable crosslinking between the chains of filipin molecules through the reaction of crosslinking agents with specific functional groups in the filipin backbones or side chains [13, 21–24].

Overall, these current strategies are essentially still about modulating the secondary structure of silk fibroin, while they are only empirical methods due to the lack of a clear law of mechanical enhancement of secondary structure. There are many natural materials with high mechanical properties in nature [25, 26] (e.g., bones, teeth, and shells), which have highly ordered nanosheet structures and continuous organic matrices. By studying these delicate structures, it can be concluded that the confinement effect and orientation of biomolecules play a key role in improving the strength, modulus, and fracture toughness of biomaterials [27–29]. This inspired us to find an alternative approach to modulate the mechanical properties of regenerated silk fibroin materials.

Here, we utilized the superspreading property of the liquid on the hydrogel surface to induce the orientation of the montmorillonite (MMT) nanosheets through the liquid shear flow, forming a highly oriented layered structure of montmorillonite nanosheets, and introduced the regenerated silk protein into the gap between the montmorillonite nanosheets. The interphase is formed by the strong interaction between the montmorillonite and the regenerated silk fibroin. Moreover, the changes in the secondary structure of regenerated silk fibroin in confined space were studied by taking advantage of the property that ethanol can induce secondary structure transformation, where random coils/α-helices/β-turns are transformed into β-crystals [30]. Due to the strong interaction between montmorillonite nanosheets and regenerated silk fibroin (hydrophobicity, hydrogen bonding, etc.), regenerated silk fibroin can form a continuous interphase on the montmorillonite surface and highly oriented confined β-crystals, which significantly enhance the mechanical properties of RSF materials. These materials exhibit excellent mechanical properties with a tensile strength of 452.31 ± 21.23 MPa and modulus of 21.67 ± 0.24 GPa, which are superior to current silk fibroin materials.

2 Experimental

2.1 Preparation of regenerated silk fibroin solutions

The RSF aqueous dispersion was prepared from *Bombyx mori* (*B. mori*) silkworm cocoons according to a further refined procedure as described by Zhang et al. [31]. Briefly, *B. mori* cocoons, supplied by Sericulture Factory (Ankang, Shanxi Province, China), were boiled in 0.5 wt.% $NaHCO_3$ solution at 100 °C for 30 min to remove the outer layer of silk gelatin. The extracted silk fibroin was dissolved in 9.3 mol/L LiBr aqueous solution at 60 °C to form a yellowish thick solution, and LiBr was removed using dialysis. The solution was centrifuged to obtain a clarified SF solution. The concentration of the silk SF was determined by dry weighing. This solution was further adjusted to 0.5 wt.% SF in aqueous solutions.

2.2 Preparation of polyacrylamide (PAAm) hydrogels containing Ca^{2+} ions

PAAm hydrogels were prepared according to the procedure described by Zhao et al. [32]. Acrylamide (15 g, monomer), N,N'-methylenebis(acrylamide) (0.3 g, crosslinker), and ammonium persulfate (0.3 g, initiator) were sequentially added to 100 mL distilled water, and completely dissolved. N,N,N',N'-tetramethylethylenediamine (300 μL, catalyst) was added to the prepared solution, and quickly poured into a mold to synthesize the PAAm hydrogel. The resulting hydrogel was immersed in 0.05 mol/L $CaCl_2$ aqueous solution for complete swelling.

2.3 Preparation of reaction solutions

The polymer and nanofiller solutions were prepared separately. A 2 wt.% sodium alginate (SA) solution was prepared by dissolving 2 g of SA powder (Sinopharm) in 98 mL deionized water, and a 2 wt.% nanosheet solution was obtained by dispersing MMT (Cloisite Na, PGW) nanosheets in deionized water. These two solutions were mixed with a 0.5 wt.% RSF solution prepared by the method described above in different ratios to prepare various reaction solutions with different mass percentages of nanofillers. The detailed mixing ratios are listed in Table S1 in the Electronic Supplementary Material (ESM).

2.4 Preparation of RSF/montmorillonite nanocomposites and post-treatment

The reaction solution (~ 3 mL) was dripped onto the PAAm hydrogel soaked with calcium ions. The reaction solution layer

gelatinized rapidly into a gel by *in situ* ionic crosslinking of SA as Ca^{2+} ions diffused from the hydrogel surface into the liquid film during the superspreading process. This gel film was easily separated from the hydrogel surface in a water bath. A trace amount of Rhodamine B dye was added to the reaction solution to facilitate observation and transfer of the thin gel film in water. It did not participate in any chemical reaction and was removed in subsequent washing and drying steps, having no effect on the structure or properties of the final composite material. After the gel films were dried in a drying oven at 60 °C and atmospheric pressure for 5 h, uniform and continuous nanocomposite films without defects were collected. According to the ratio of MMT/(MMT + RSF), the corresponding nanocomposites were named as N-0%, N-10%, N-20%, N-30%, N-40%, and N-50%, e.g., N-30% means that the MMT/(MMT + RSF) in the solution was 30%. The specific feeding ratios are listed in Table S1 in the ESM. To induce the formation of β-crystals in the confined space, all dried films were further immersed in 80 vol.% aqueous ethanol solutions for 30 min. The post-treated films were designated E-0%, E-10%, E-20%, E-30%, E-40%, and E-50%, respectively.

2.5 Morphology observation

All samples were bonded with conductive adhesive and coated with gold by vacuum sputtering on a gold target for 30 s. The cross-sectional morphology of the samples was observed by scanning electron microscopy (SEM) at a voltage of 5 kV.

2.6 Mechanical tests of nanocomposite films

Rectangular strips (1 mm wide and 10 mm long) of the laminated samples were tested at a rate of 0.5 mm/min using a Mark-10 Corporation mechanical strength tester (ESM 303) to obtain stress–strain curves. The thickness of all samples was measured using SEM's Image J software.

2.7 Fourier transform infrared (FTIR) spectroscopy

The infrared spectra of the samples in the wavelength range of 600 to 4000 cm^{-1} were recorded on an iCAN 9 FTIR spectrometer (Tianjin Neng Spectrum Technology Co., Ltd., China). The amide I band of the spectra (1600–1700 cm^{-1}) was back-convolved using PeakFit software for quantitative analysis of the secondary structure content. The secondary structure content was quantified by deconvoluting the vibrational peaks of the amide groups (1600–1700 cm^{-1}) of the spectra using PeakFit software.

2.8 Atomic force microscopy (AFM)

The topography of the samples was obtained by tapping mode AFM (Bruker Multimode 8) scanning with a rectangular silicon cantilever beam (RTESP, Bruker) with a resonance frequency of 300 kHz, a spring constant of 40 N/m, and a tip radius of 10 nm.

2.9 Small-angle X-ray scattering (SAXS)

The aggregation state of the nanofillers in the polymer matrix was investigated by SAXS. The specific experimental parameters were as follows: the thickness of the sample was 1 mm, the length of the sample was 30 mm, the width of the sample was a long strip of 5 mm, the distance between the sample and the detector was 5 m, and the experimental time was 15 min.

2.10 Enzymatic degradation

The RSF nanocomposites were weighed and placed in 1 wt.% phosphate buffered saline (PBS) solution, and the shaker temperature was set at 35 °C. The enzyme solution was replaced every 3 days, and a control group of PBS solution without enzyme was set up. The samples were freeze-dried and weighed to calculate the degradation rate after 1, 3, 5, 7, 10, 14, 18, and 21 days of degradation, respectively.

3 Results and discussion

3.1 Preparation strategy of regenerated silk fibroin nanocomposites

Firstly, we used the common LiBr solubilization system to convert fibrous silk fibroin into aqueous solutions of RSF (Fig. 1(a)). RSF, MMT nanosheets, and SA were mixed to form a reaction solution, and this solution was added dropwise to the surface of a PAAm hydrogel containing calcium ions (Ca^{2+}). During this process, the reactive solution droplets will undergo super spreading behavior (Fig. 1(b)) [32]. To directly observe this spreading process, we recorded the spreading behavior of the droplets on the hydrogel surface using high-speed camera images. As shown in Fig. S1(a) in the ESM, the droplets spread rapidly and completely within 600 ms after contacting the gel surface, which can shear-induce the nanosheets in the system to form highly oriented structures. At the same time, SA in the reaction solution will combine with Ca^{2+} in the PAAm hydrogel to realize *in situ* crosslinking to form hydrogels with highly oriented structures (Fig. 1(b)). These gels were dried in a drying oven at 60 °C for 5 h to obtain RSF nanocomposites with highly oriented laminar structure, seen in the scanning electron microscope photographs (inset of Fig. 1(b)). It is worth mentioning that these materials can also be prepared in large area, as shown in Fig. S1(b) in the ESM. Furthermore, we further used ethanol to induce secondary structure transformation, where random coils/α-helices/β-turns are transformed into β-crystals.

3.2 Characterization of MMT nanosheet, RSF, and RSF nanocomposite morphology

AFM was used to characterize the morphology of MMT nanosheets and RSF in the prepared solutions. MMT nanosheets are mainly stacked together by electrostatic interaction between layers, and the surface contains abundant hydroxyl groups [33] (Fig. 2(a)). As shown in Fig. 2(c), the lateral size of the MMT nanosheets is on the order of several hundred nanometers, and the thickness measured by AFM is approximately 1.4 nm, indicating that the MMT nanosheets are well dispersed in the solution, with no stacking or aggregation observed. RSF has a multi-level secondary structure, which is manifested by amino acid sequences (glycine–alanine–glycine–alanine–glycine–serine (GAGAGS)) [34] consisting of β-folded secondary structures that further form β-crystal networks (Fig. 2(b)). During the drying process, the RSF begins to aggregate. Figure 2(d) shows that RSF molecules form irregularly sized micelles with lengths of 50–90 nm and heights of 3–5 nm due to chain folding and hydrophobic interactions [35].

To characterize the morphology of the RSF nanocomposites, we observed their cross-section using SEM images. As shown in Fig. 2(e), the layered structure of RSF nanocomposite becomes more pronounced as the MMT content increases. In the N-0% sample without MMT nanosheets, the cross-section is uneven with a thickness of about 3 μm. In the N-10% sample, a small amount of nanosheets can be observed in the cross-section. As the nanosheet

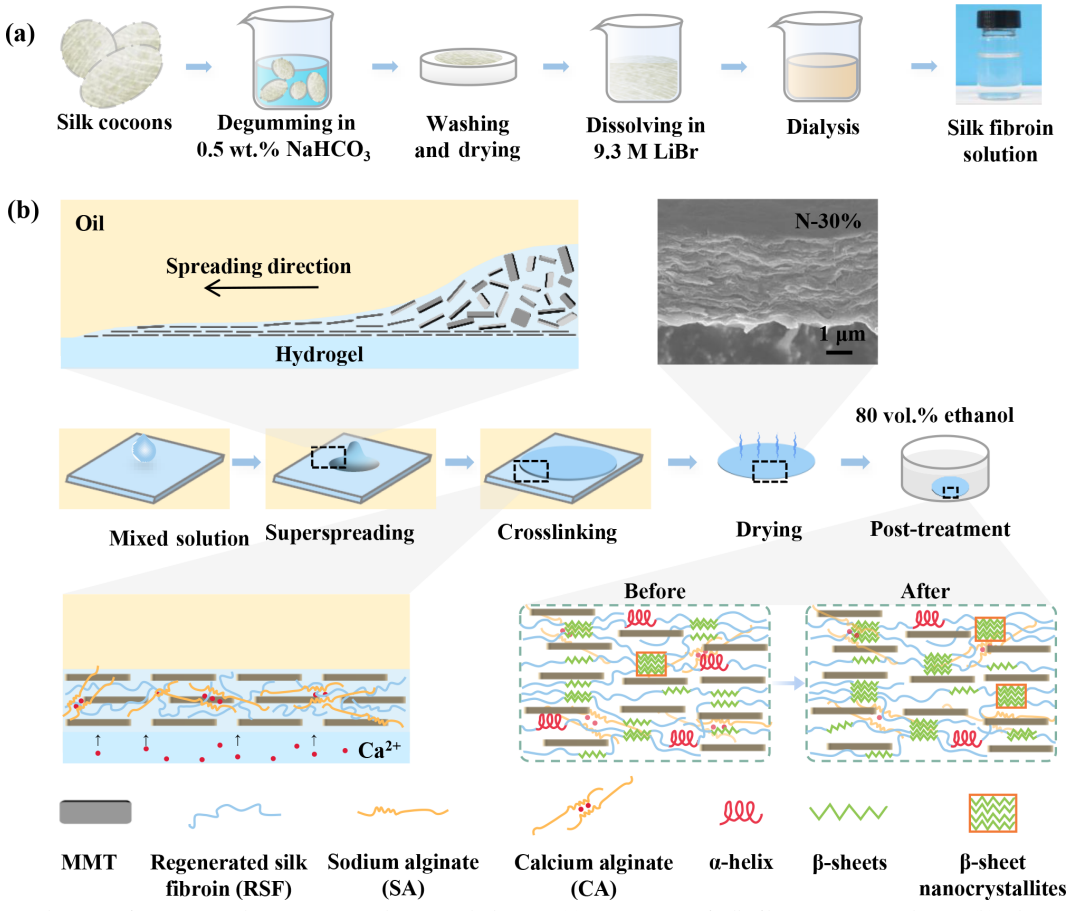

Figure 1 Schematic diagram of RSF material preparation and structural changes. (a) Preparation of silk fibroin aqueous solution. (b) The general strategy for constructing RSF nanocomposites with high mechanical properties by introducing oriented nanoconfined β-crystals.

content is 20–30, these samples (N-20% and N-30%) show highly ordered laminar structure. The section of the N-50% sample also has an obvious layered structure, but the direction of the nanosheets in the middle part is at an angle to the horizontal direction. This is due to the high percentage of MMT nanosheets in the composite film, forming a small number of agglomerates. To verify the successful introduction of RSF into the nanoconfined space created by MMT sheets during the superspreading process, we performed energy dispersive X-ray spectroscopy (EDS) characterization of the N-30% sample (Fig. S2 in the ESM). We clearly observe that the distribution of all elements is showing a lamellar structure. N and Ca elements are concentrated in the nanosheets, indicating that RSF is successfully introduced into the nanosheets and crosslinks are formed. The boundaries of Si element distribution are highly coincident with the boundaries of lamellar structure of RSF nanocomposites, which indicates that the Si elements originate from MMT nanosheets.

We further used SAXS to investigate the orientation structure of the RSF nanocomposites. All samples containing nanosheets showed anisotropic characteristics (Figs. 3(a) and 3(b)). We calculated the orientation factors of the RSF nanocomposites with different nanosheet contents [36], which were all around 0.8, indicating that all the samples were highly oriented (Fig. 3(e)). The slight decrease in the orientation factor with increasing MMT content is likely due to enhanced nanosheet interactions at high contents, which introduce minimal local deflections or ripples during film formation, even in structures with overall high orientation [32]. This is consistent with some irregular layered structures observed in the SEM images of N-50% samples (Fig. 2(e)). The high orientation of the nanosheets in the RSF nanocomposites is mainly due to the shear force generated during the superspreading process.

To analyze the effect of the oriented lamellar structure on the mechanical properties, we systematically characterized the mechanical behavior of samples with different nanosheet contents. Figure 3(c) shows the stress–strain curves of RSF nanocomposites with different MMT nanosheet content. It is clear that the mechanical properties improve significantly with increasing nanosheet content. At a nanosheet content of 30%, the RSF nanocomposite shows optimal mechanical properties. As the nanosheet content is further increased, the mechanical properties instead show a decrease. Figure 3(f) further quantifies this trend by showing the changes in strength and modulus with varying nanosheet content. Strength and modulus reach their maximum at 30% nanosheet content and then decrease, but remain at a relatively high level overall. The N-30% sample has a strength of 237.12 ± 20.54 MPa and a modulus of 14.48 ± 0.05 GPa, which are about 5 and 2 times that of pure RSF, respectively. This indicates that the performance of the RSF nanocomposites can be significantly improved by optimizing the nanosheet content. The strength and modulus of the N-40% and N-50% samples are much lower than that of the N-30% sample, which is due to the high content of nanosheets in these systems, where partial agglomeration occurs. We treated these nanocomposites with ethanol solutions to induce

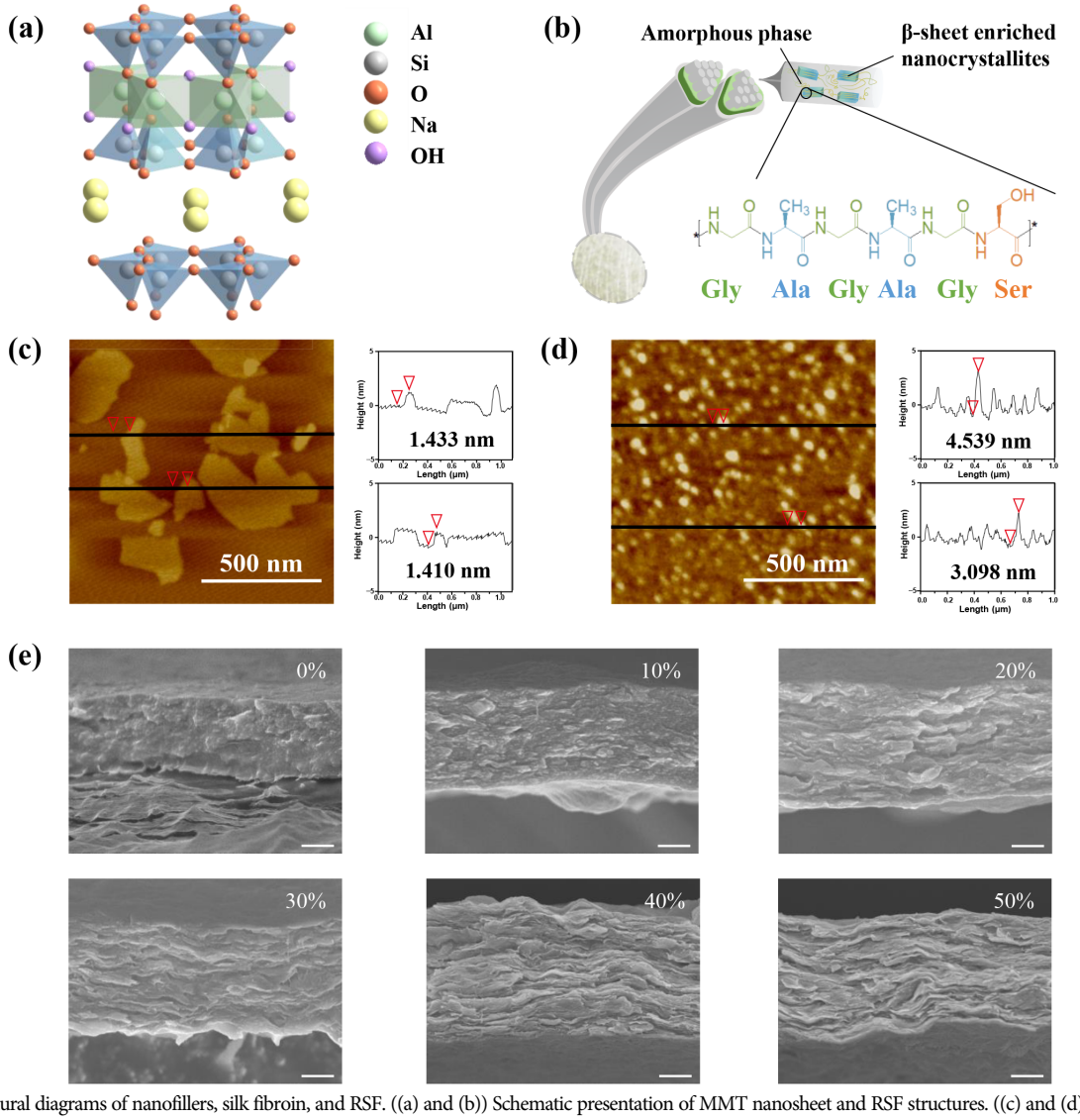

Figure 2 Structural diagrams of nanofillers, silk fibroin, and RSF. ((a) and (b)) Schematic presentation of MMT nanosheet and RSF structures. ((c) and (d)) AFM images of the MMT nanosheets and RSF. (e) SEM images of RSF nanocomposites, scale bars: 1 μm.

β-crystal formation of RSF and further improve their mechanical properties (Figs. 3(d) and 3(g)). After the treatment with ethanol solution, the mechanical properties of RSF nanocomposites were significantly improved, with the highest strength and modulus reaching 452.31 ± 21.23 and 21.67 ± 0.24 GPa, respectively. Compared to existing reported RSF nanocomposites [33, 37–40], our materials exhibit superior strength and toughness (Fig. 3(h) and Table S2 in the ESM). Furthermore, compared to traditional commercial plastics (e.g., poly(vinyl chloride) (PVC), polyethylene (PE), polycarbonate, styrene, and polymethylmethacrylate), our materials also show the optimal strength and modulus (Fig. 3(i) and Table S3 in the ESM). This indicates that RSF nanocomposites with highly oriented structures have great potential to replace plastics.

To reveal the mechanical enhancement of such a design for RSF nanocomposites, we first investigated the role of confined effects of nanosheet formation. The RSF molecule contains mainly four types of secondary structures: α-helix, β-crystal, β-turning, and random coil, and these secondary structures have corresponding characteristic peaks in the infrared spectra. By performing Fourier deconvolution on the infrared absorption peaks in a specific wave number range, the relative content of each secondary structure in RSF nanocomposites can be quantitatively analyzed. As shown in Fig. S3(a) in the ESM, the characteristic peaks at 1242, 1332, 1525, and 1651 cm^{-1} on the infrared spectrum are the random curling, α-helix, β-sheet, and random curling/α-helix. We used Peak Fit software with wave numbers between 1600–1700 cm^{-1} amide absorption peaks for peak fitting calculations to derive the secondary structure content of RSF in the nanocomposites with different MMT sheet contents (Fig. S3 in the ESM). Figure 4(a) shows the variation of the secondary structure content of RSF nanocomposites with different MMT nanosheet contents. The β-sheet content in the composites first increases and then decreases with the nanosheet content. Moreover, RSF nanocomposites exhibit higher thermal stability than pure RSF (Fig. 4(b)). We characterized the aggregated state of MMT nanosheets using SAXS. As shown in Fig. 4(c), with increasing nanosheet content, the intensity peak corresponding to the average interlayer distance (d) shifts to the high diffraction vector (q) region. According to the Bragg equation $d = 2\pi/q$ peak, the interlayer distance can be calculated and statistically plotted in Fig. 4(d). The nanosheet content was increased from 10% to 50%, and the interlayer distance was decreased from 5.46 to 2.21 nm, indicating that the limiting domain

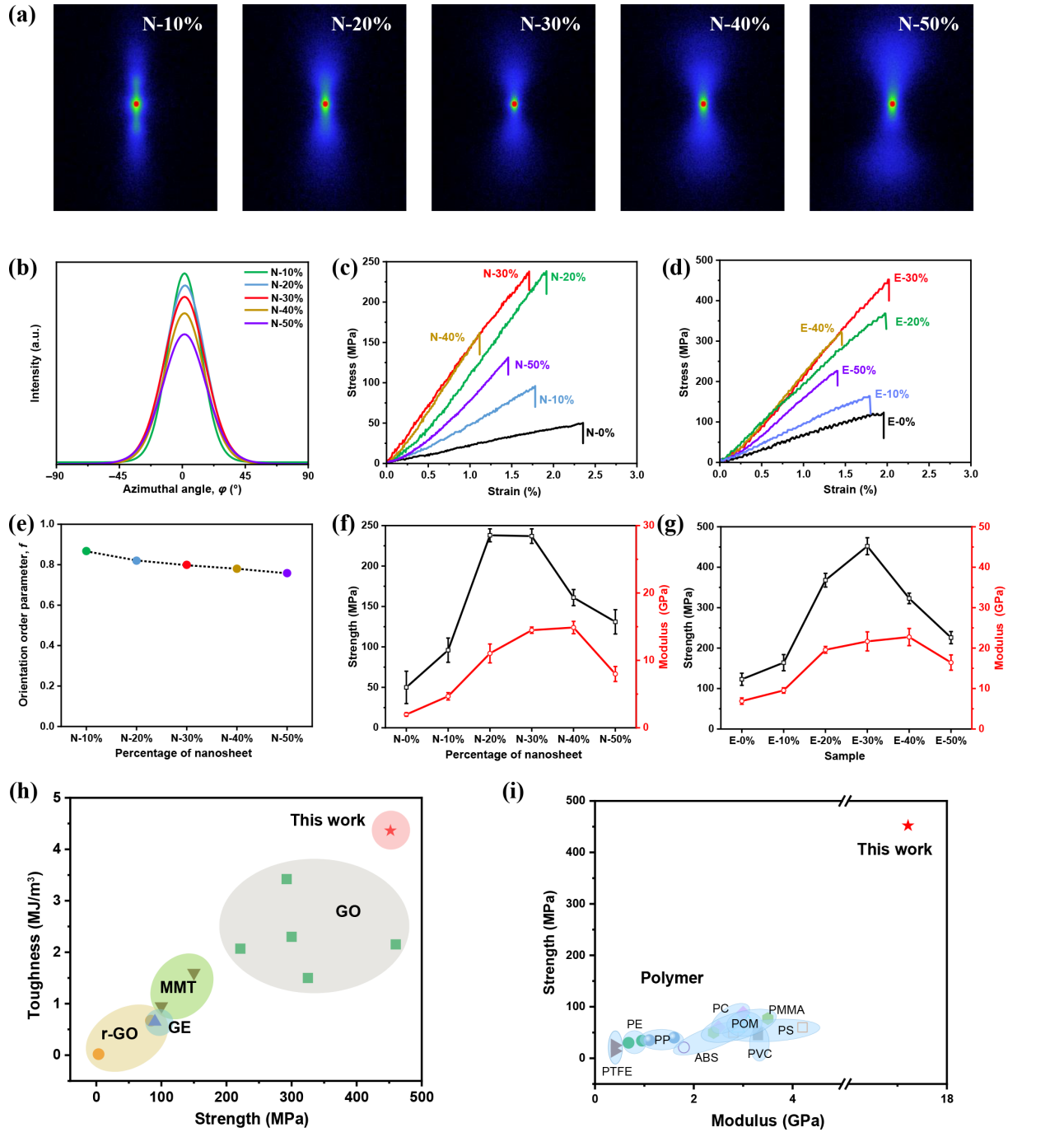

Figure 3 Orientation and mechanical property characterization of pure RSF and RSF materials with alcohol treatment. (a) SAXS images of RSF nanocomposites with different MMT nanosheet contents. ((b) and (e)) Plots of azimuthal angle (φ) and the orientation order parameter of RSF nanocomposites prepared by the superspreading strategy. ((c) and (f)) Tensile stress–strain curves and strength and modulus of RSF nanocomposites with different MMT nanosheet contents. ((d) and (g)) Tensile stress–strain curves and strength and modulus of RSF nanocomposites with different MMT nanosheet contents after alcohol solution treatment. ((h) and (i)) Mechanical properties of RSF nanocomposites compared to current silk-based nanocomposites and commercialized plastics.

space size can be modulated by controlling the nanosheet content. We also took transmission electron micrographs of the N-30% sample. As shown in Fig. 4(e), the MMT nanosheets are well oriented, and their layer spacing is consistent with that obtained from SAXS experimental calculations (4.23 nm). We labeled the β-crystals formed in the interlayer of MMT nanosheets, and used Gatan Digital Micrograph software to perform a Fourier transform of the selected area to measure the spacing of the β-crystals in the N-30% sample, which was approximately 0.43 nm, corresponding to the [200]/[210] lattice planes, in agreement with Refs. [41, 42] (Fig. 4(f) and Fig. S4 in the ESM). Based on our results, we proposed the oriented nanoconfined β-crystals of RSF nanocomposites to enhance mechanical properties (shown in Fig. 4(g)). When the MMT nanosheet content is low, the interlayer distance is so large that the weak interaction is not sufficient to cause the RSF segment to move. As the MMT nanosheet content further increases, there are various supramolecular interactions between the nanosheets and the silk, such as electrostatic,

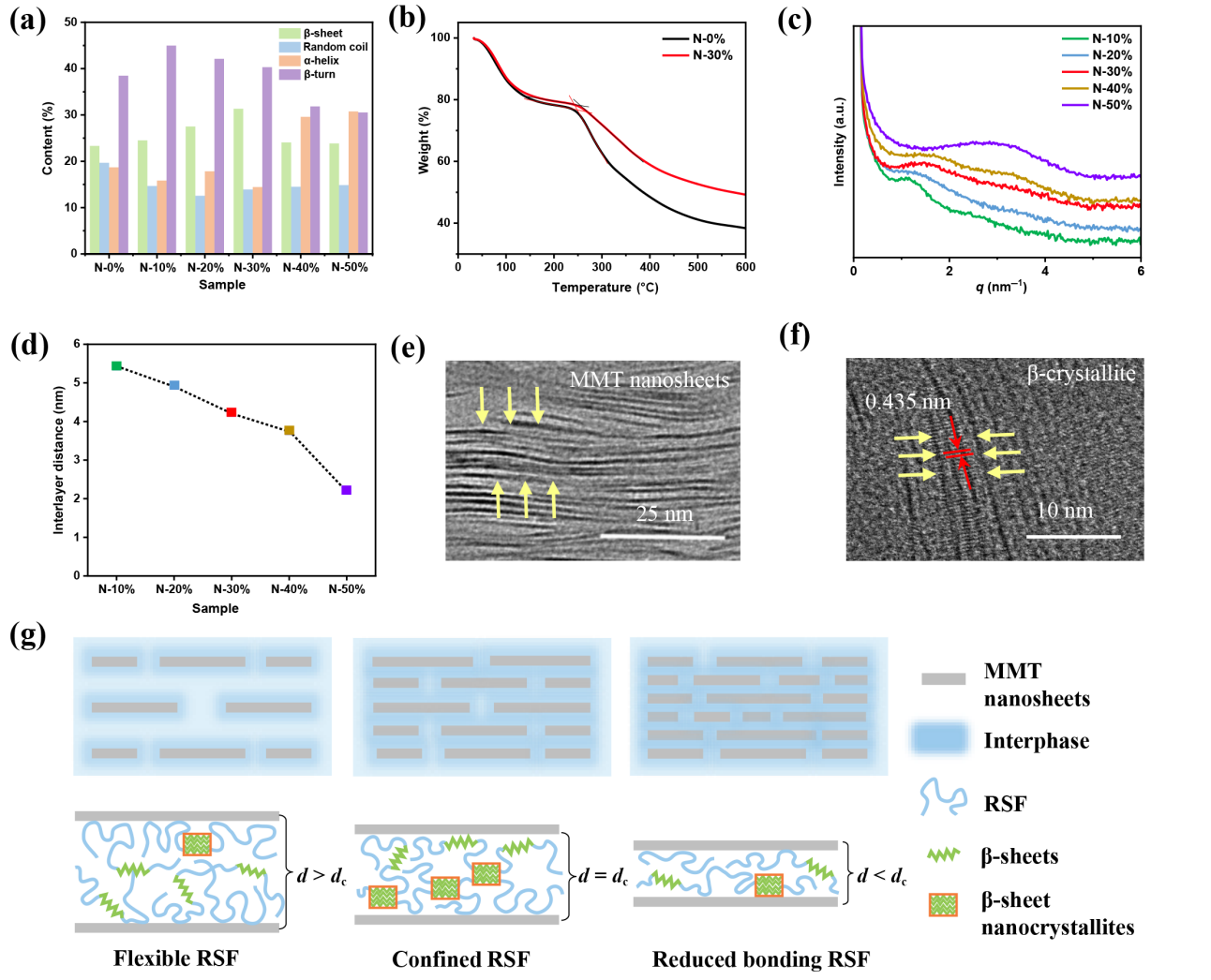

Figure 4 Characterization of secondary structure changes in pure RSF materials with the confined space. (a) Relative content of each secondary structure, (b) thermogravimetric curves, (c) plots of diffraction vector, and (d) interlayer distances of RSF nanocomposites with different MMT nanosheet contents. ((e) and (f)) TEM images of N-30% RSF nanocomposite and β-crystals. (g) Schematic diagram illustrating the oriented nanoconfined β-crystals between the aligned nanosheets at different interlayer distances.

hydrophilic, and hydrogen bonding, which are conducive to the formation of the β-folded conformation. Furthermore, the well-aligned MMT nanosheets form two-dimensional nanochannels with tunable interlayer spacing (Figs. 4(d) and 4(g)). This confined geometry physically restricts the conformational entropy of the RSF chains, promoting their alignment and facilitating the nucleation and directional growth of β-sheets along the nanosheet surface. Therefore, it is clear that this long-range ordered structure of MMT nanosheets and confined RSF β-sheets is the key to improving mechanical properties of the nanocomposites. However, excessively high MMT nanosheet content restricts the movement of the RSF chains, resulting in a decrease in the β-sheet content and mechanical performance. An appropriate nanosheet content provides effective physical confinement and interfacial area for the formation of β-crystals, without causing nanosheet aggregation (reducing the effective interface) and excessively restricting the chain segment movement required for structural reorganization.

While the current strategy of constructing oriented nanoconfined β-sheet crystals successfully yields regenerated silk fibroin nanocomposites with outstanding tensile strength and modulus, the elongation at break remains relatively limited, reflecting the well-known trade-off between strength and ductility in highly aligned polymer nanocomposites [26, 32, 33]. This reduced ductility primarily arises from the dense, continuous β-crystal network and strong interfacial interactions, which facilitate efficient stress transfer but restrict large-scale polymer chain mobility and plastic deformation. We believe that several approaches can be explored to overcome this limitation in future research. The first method is to introduce hierarchical structures, such as combining the current oriented lamellae with a more ductile elastomeric phase, thereby controlling the partial crystallization to balance β-sheet content and chain mobility. The second method is to construct dual or interpenetrating networks to achieve complementarity between the elastic polymer network and the rigid crystal network. Third, reversible and sacrificial bonds, such as metal-ligand coordination and dynamic covalent bonds, can be introduced to enhance additional energy dissipation. In summary, these strategies may pave the way for developing silk-based composites with high strength, high modulus, and high toughness, which is also part of our future work prospects.

We further investigated the mechanism of mechanical property enhancement of RSF nanocomposites by ethanol solution

treatment. We used SEM to characterize the cross-sectional morphology of RSF composites with different MMT nanosheet contents after ethanol solution treatment, as shown in Fig. S5 in the ESM. The overall morphology of all samples did not change significantly from that of the pretreatment period (Fig. 2(e)). Figure 5(a) shows the wide-angle X-ray diffraction (WAXD) patterns of RSF nanocomposites before and after ethanol solution treatment. The three diffraction peaks at 0.725 nm (12.2°), 0.45 nm (19.7°), and 0.316 nm (28.2°) are attributed to the randomly curled secondary structure, while the three diffraction peaks at 0.469 nm (18.9°), 0.43 nm (20.7°), and 0.36 nm (24.7°) are attributed to the β-crystal secondary structure [41–43].

It can be observed that the crystallinity of the treated RSF composites is significantly improved. In the pure RSF system (N-0% and E-0%), although the content of β-crystals increased significantly after treatment with alcohol solution, the β-crystals could not be transformed into ordered crystals due to the lack of confinement of oriented nanosheets and were distributed in the system in a disordered arrangement (Fig. 5(c) and Fig. S6 in the ESM). Imaging the orientation of β-sheet nanocrystals directly at the molecular level using transmission electron microscopy (TEM) is extremely challenging. We compared the cases where the X-ray beam was parallel and perpendicular to the film plane using WAXD. When the X-rays were parallel to the film plane, a distinct two-dimensional scattering feature was detected (Fig. S6 in the ESM). This anisotropy suggests that the nanocrystals have a preferred in-plane orientation (Fig. 5(c)). In order to quantitatively analyze the secondary structure transitions in the post-treated RSF nanocomposites, we still used infrared spectroscopy to characterize them (Fig. 5(b) and Fig. S7 in the ESM). The β-sheet content in all RSF nanocomposite samples after treatment was about 2 times higher than before treatment. In addition, N-0% and N-30% samples before treatment had more obvious peaks representing α-helix at 1651 cm^{-1}, and both E-0% and E-30% samples after treatment had obvious peaks representing β-sheet at 1624 cm^{-1}. The shift of the wave number from 1651 to 1624 cm^{-1} proved that the ethanol solution could successfully induce the transformation of the RSF secondary structure.

To investigate the degradation properties of RSF nanocomposites, we selected protease XIV and used phosphate buffer solution without protease XIV enzyme as a control group to study the degradation of three RSF nanocomposites [44, 45], namely, N-0%, N-30%, and E-30%, over a period of 21 days, as

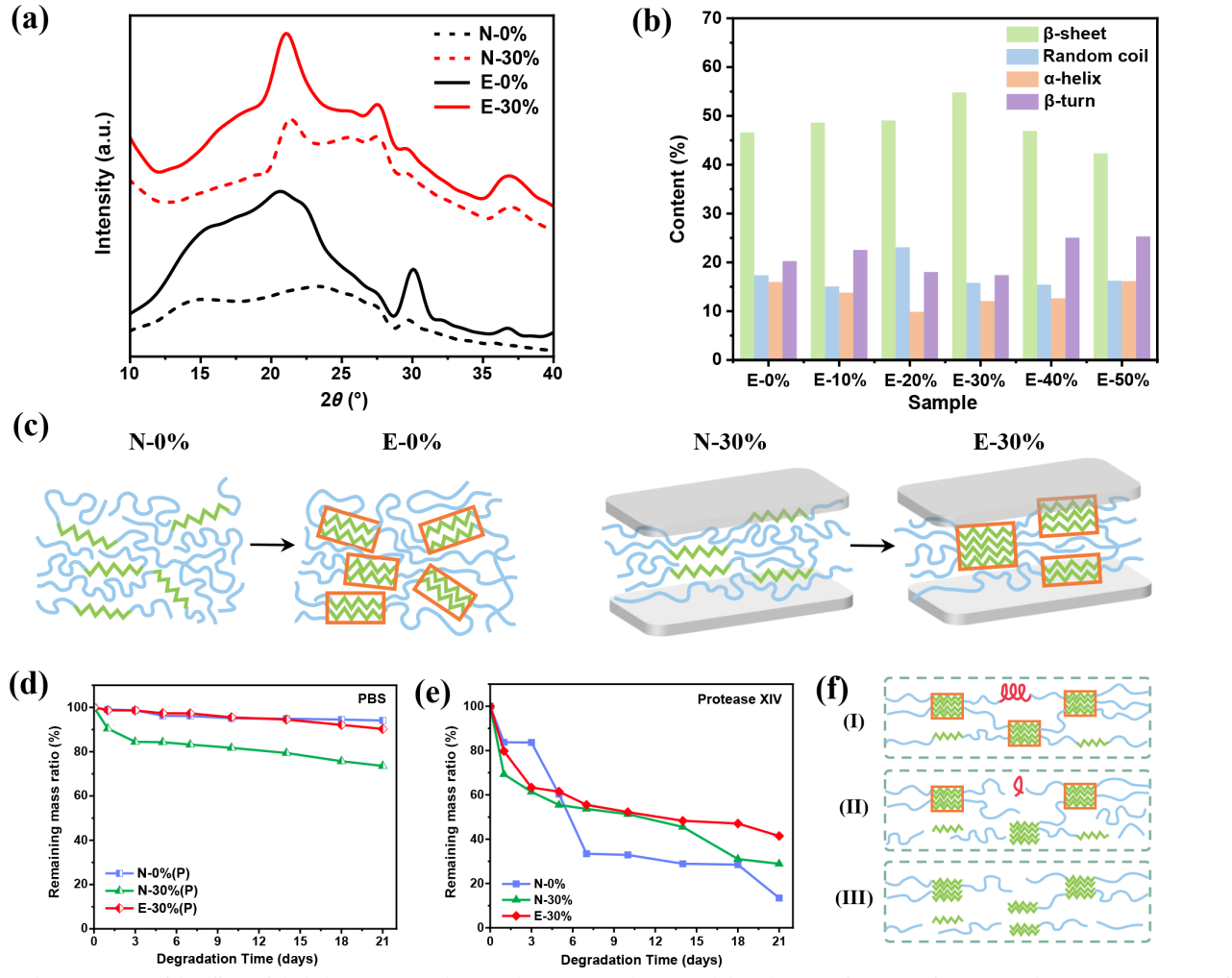

Figure 5 Characterization of the effects of alcohol treatment on the secondary structure changes and degradation performance of RSF materials. (a) WAXD patterns of RSF nanocomposites before and after treatment with alcohol solution. (b) Relative content of each secondary structure of RSF nanocomposites with different MMT nanosheet contents after treatment with alcohol solution. (c) Schematic representation of the secondary structure evolution of RSF nanocomposites before and after treatment with alcohol solution. ((d) and (e)) Degradation behavior of RSF nanocomposites in PBS buffer solutions with and without protease XIV enzyme. (f) Schematic degradation mechanism of RSF nanocomposites.

shown in Figs. 5(d) and 5(e). In the control group, after 21 days of degradation, the mass of the N-0% and E-30% samples was maintained at more than 90%, while the N-30% sample lost about 20% of its mass, which could be attributed to the presence of loosely bound RSF located on the surface of the MMT, dislodged under the action of external oscillations. For RSF nanocomposites immersed in the enzyme solution, all samples showed a significant mass loss during the initial degradation stage, which could be attributed to the disruption of the randomly curled secondary structure in the RSF. As the degradation time further increased, the presence of a large number of β-crystals slowed down the enzymatic degradation process (Fig. 5(f)). It is worth mentioning that RSF nanocomposites degrade significantly slower than pure RSF, which further suggests that the confinement effect of nanosheets can improve the stability of β-crystals.

4 Conclusions

In conclusion, we successfully constructed RSF nanocomposites with a highly oriented layered structure of montmorillonite nanosheets by super-spreading strategy, and investigated the structural changes of RSF nanocomposites under different layer spacings. Their mechanical properties can be significantly enhanced by nanoconfined β-crystals of RSF in the two-dimensional nanoconfined space of montmorillonite nanosheets. Meanwhile, we treated RSF nanocomposites with an alcohol solution to further increase the amount of their nanoconfined β-crystals. These materials exhibit excellent mechanical properties with a tensile strength of 452.31 ± 21.23 MPa and modulus of 21.67 ± 0.24 GPa, superior to current silk fibroin materials. It is worth mentioning that these materials have good degradability in the presence of enzymes, and the large-scale preparation can be realized using our superspreading strategy, which expands the practical application of RSF nanocomposites.

Electronic Supplementary Material: Supplementary material (further details of the spreading process, SEM and TEM measurements, FTIR spectroscopy measurements, wide-angle X-ray diffraction measurements, specific experimental ratios, and mechanical data) is available in the online version of this article at https://doi.org/10.26599/NR.2026.94908475.

Data availability

All data needed to support the conclusions in the paper are presented in the manuscript and the Electronic Supplementary Material. Additional data related to this paper may be requested from the corresponding author upon request.

Acknowledgements

This work was supported by the Postdoctoral Research Funding of Hangzhou International Innovation Institute of Beihang University (No. 2025BKZ007), the National Key Research and Development Program of China (Nos. 2022YFA1503000 and 2022YFA1503004), and the National Natural Science Foundation of China (Nos. 22175010 and 22403006).

Declaration of competing interest

All the contributing authors report no conflict of interests in this work.

Author contribution statement

H. S. Z. and Y. F. R.: Data curation, project administration, validation, writing manuscript, experimental design. H. F. and H. Z.: Data curation, project administration, validation, experimental design. C. Z., L. X. L., and C. Q. Z.: Project administration, writing manuscript. H. S. Z., J. H. and M. J. L.: Project administration, funding acquisition, writing manuscript. All the authors have approved the final manuscript.

Use of AI statement

None.

References

[1] Geyer, R.; Jambeck, J. R.; Law, K. L. Production, use, and fate of all plastics ever made. *Sci. Adv.* **2017**, *3*, e1700782.

[2] Li, C. M.; Wu, J. Q.; Shi, H. Y.; Xia, Z. Y.; Sahoo, J. K.; Yeo, J.; Kaplan, D. L. Fiber-based biopolymer processing as a route toward sustainability. *Adv. Mater.* **2022**, *34*, 2105196.

[3] Pei, Y.; Wang, L.; Tang, K. Y.; Kaplan, D. L. Biopolymer nanoscale assemblies as building blocks for new materials: A review. *Adv. Funct. Mater.* **2021**, *31*, 2008552.

[4] Koh, L. D.; Cheng, Y.; Teng, C. P.; Khin, Y. W.; Loh, X. J.; Tee, S. Y.; Low, M.; Ye, E. Y.; Yu, H. D.; Zhang, Y. W. et al. Structures, mechanical properties and applications of silk fibroin materials. *Prog. Polym. Sci.* **2015**, *46*, 86–110.

[5] Shao, Z. Z.; Vollrath, F. Surprising strength of silkworm silk. *Nature* **2002**, *418*, 741–741.

[6] Hardy, J. G.; Römer, L. M.; Scheibel, T. R. Polymeric materials based on silk proteins. *Polymer* **2008**, *49*, 4309–4327.

[7] Ma, L. Y.; Liu, Q.; Wu, R. H.; Meng, Z. H.; Patil, A.; Yu, R.; Yang, Y.; Zhu, S. H.; Fan, X. W.; Hou, C. et al. From molecular reconstruction of mesoscopic functional conductive silk fibrous materials to remote respiration monitoring. *Small* **2020**, *16*, 2000203.

[8] Matsumoto, K.; Uejima, H.; Iwasaki, T.; Sano, Y.; Sumino, H. Studies on regenerated protein fibers. III. Production of regenerated silk fibroin fiber by the self-dialyzing wet spinning method. *J. Appl. Polym. Sci.* **1996**, *60*, 503–511.

[9] Ishizaka, H.; Watanabe, Y.; Ishida, K.; Fukumoto, O. Regenerated silk prepeared from ortho phosphoric acid solution of fibroin. *J. Insect Biotechnol. Sericol.* **1989**, *58*, 87–95.

[10] Liu, X. Y.; Zhang, C. C.; Xu, W. L.; Liu, H. T.; Ouyang, C. X. Blend films of silk fibroin and water-insoluble polyurethane prepared from an ionic liquid. *Mater. Lett.* **2011**, *65*, 2489–2491.

[11] Zhang, F.; Lu, Q.; Ming, J. F.; Dou, H.; Liu, Z.; Zuo, B. Q.; Qin, M. D.; Li, F.; Kaplan, D. L.; Zhang, X. G. Silk dissolution and regeneration at the nanofibril scale. *J. Mater. Chem. B* **2014**, *2*, 3879–3885.

[12] Wang, C. Y.; Xia, K. L.; Zhang, Y. Y.; Kaplan, D. L. Silk-based advanced materials for soft electronics. *Acc. Chem. Res.* **2019**, *52*, 2916–2927.

[13] Kim, M. H.; Park, W. H. Chemically cross-linked silk fibroin hydrogel with enhanced elastic properties, biodegradability, and biocompatibility. *Int. J. Nanomed.* **2016**, *11*, 2967–2978.

[14] Farokhi, M.; Aleemardani, M.; Solouk, A.; Mirzadeh, H.; Teuschl, A. H.; Redl, H. Crosslinking strategies for silk fibroin hydrogels: Promising biomedical materials. *Biomed. Mater.* **2021**, *16*, 022004.

[15] Lu, L.; Fan, S. N.; Geng, L. H.; Lin, J. Y.; Yao, X.; Zhang, Y. P. Flow analysis of regenerated silk fibroin/cellulose nanofiber suspensions via a bioinspired microfluidic chip. *Adv. Mater. Technol.* **2021**, *6*, 2100124.

[16] Hu, X.; Shmelev, K.; Sun, L.; Gil, E. S.; Park, S. H.; Cebe, P.; Kaplan,

D. L. Regulation of silk material structure by temperature-controlled water vapor annealing. *Biomacromolecules* **2011**, *12*, 1686–1696.

[17] Chen, H. W.; Lin, M. F.; Lai, Y. H.; Chen, B. Y. Skin-friendly dressing with alcohols treatment for enhancement of mechanical and biocompatible properties. *J. Taiwan Inst. Chem. Eng.* **2021**, *129*, 256–263.

[18] Wang, Y. X.; Ma, R. L.; Hu, K. S.; Kim, S.; Fang, G. Q.; Shao, Z. Z.; Tsukruk, V. V. Dramatic enhancement of graphene oxide/silk nanocomposite membranes: Increasing toughness, strength, and Young's modulus via annealing of interfacial structures. *ACS Appl. Mater. Interfaces* **2016**, *8*, 24962–24973.

[19] Um, I. C.; Kweon, H.; Park, Y. H.; Hudson, S. Structural characteristics and properties of the regenerated silk fibroin prepared from formic acid. *Int. J. Biol. Macromol.* **2001**, *29*, 91–97.

[20] Su, D. H.; Yao, M.; Liu, J.; Zhong, Y. M.; Chen, X.; Shao, Z. Z. Enhancing mechanical properties of silk fibroin hydrogel through restricting the growth of β-sheet domains. *ACS Appl. Mater. Interfaces* **2017**, *9*, 17489–17498.

[21] Zheng, H. Y.; Zuo, B. Q. Functional silk fibroin hydrogels: Preparation, properties and applications. *J. Mater. Chem. B* **2021**, *9*, 1238–1258.

[22] Das, S.; Pati, F.; Choi, Y. J.; Rijal, G.; Shim, J. H.; Kim, S. W.; Ray, A. R.; Cho, D. W.; Ghosh, S. Bioprintable, cell-laden silk fibroin-gelatin hydrogel supporting multilineage differentiation of stem cells for fabrication of three-dimensional tissue constructs. *Acta Biomater* **2015**, *11*, 233–246.

[23] McGill, M.; Coburn, J. M.; Partlow, B. P.; Mu, X.; Kaplan, D. L. Molecular and macro-scale analysis of enzyme-crosslinked silk hydrogels for rational biomaterial design. *Acta Biomater.* **2017**, *63*, 76–84.

[24] Mu, X.; Sahoo, J. K.; Cebe, P.; Kaplan, D. L. Photo-crosslinked silk fibroin for 3D printing. *Polymers* **2020**, *12*, 2936.

[25] Wei, J. J.; Pan, F.; Ping, H.; Yang, K.; Wang, Y. Q.; Wang, Q. Y.; Fu, Z. Y. Bioinspired additive manufacturing of hierarchical materials: From biostructures to functions. *Research* **2023**, *6*, 0164.

[26] Zhou, H. S.; Zha, H.; Zhang, Z. Z.; Huang, J.; Liu, M. J. Advanced mechanical polymer nanocomposites: From confined interphase to structural synergy. *Chem. Commun.* **2025**, *61*, 16132–16149.

[27] Kong, S. W.; Zhao, C. Q.; Sun, Y. Z.; Huang, J.; Zhang, L. H.; Ru, Y. F.; Zhou, H. S.; Zhou, T. X.; Liu, M. J. Large-area, high-strength cellulose nanocomposites enhanced by confined polymer nanocrystallization in Bouligand structures. *Matter* **2024**, *7*, 2250–2264.

[28] Xu, Y. C.; Huang, Y. Z.; Yan, H.; Gu, Z. D.; Zhao, T. Y.; Zhang, R.; Pan, B.; Dong, L. T.; Liu, M. J.; Jiang, L. Sunflower-pith-inspired anisotropic auxetic mechanics from dual-gradient cellular structures. *Matter* **2023**, *6*, 1569–1584.

[29] Zhou, H. S.; Huang, J.; Zhao, T. Y.; Liu, M. J. Bioinspired composite polymeric gel with multiphase confinement. *Acta Polym. Sin.* **2023**, *54*, 1641–1662.

[30] Li, M. Z.; Tao, W.; Kuga, S.; Nishiyama, Y. Controlling molecular conformation of regenerated wild silk fibroin by aqueous ethanol treatment. *Polym. Adv. Technol.* **2003**, *14*, 694–698.

[31] Zhang, X. Y.; Xiao, L. Y.; Ding, Z. Z.; Lu, Q.; Kaplan, D. L. Fragile-tough mechanical reversion of silk materials via tuning supramolecular assembly. *ACS Biomater. Sci. Eng.* **2021**, *7*, 2337–2345.

[32] Zhao, C. Q.; Zhang, P. C.; Zhou, J. J.; Qi, S. H.; Yamauchi, Y.; Shi, R. R.; Fang, R. C.; Ishida, Y.; Wang, S. T.; Tomsia, A. P. et al. Layered nanocomposites by shear-flow-induced alignment of nanosheets. *Nature* **2020**, *580*, 210–215.

[33] Kharlampieva, E.; Kozlovskaya, V.; Wallet, B.; Shevchenko, V. V.; Naik, R. R.; Vaia, R.; Kaplan, D. L.; Tsukruk, V. V. Co-cross-linking silk matrices with silica nanostructures for robust ultrathin nanocomposites. *ACS Nano* **2010**, *4*, 7053–7063.

[34] Wu, R. H.; Ma, L. Y.; Liu, X. Y. From mesoscopic functionalization of silk fibroin to smart fiber devices for textile electronics and photonics. *Adv. Sci.* **2022**, *9*, 2103981.

[35] Chen, P.; Kim, H. S.; Park, C. Y.; Kim, H. S.; Chin, I. J.; Jin, H. J. pH-triggered transition of silk fibroin from spherical micelles to nanofibrils in water. *Macromol. Res.* **2008**, *16*, 539–543.

[36] Zhou, T. X.; Zhao, C. Q.; Liu, Y. H.; Huang, J.; Zhou, H. S.; Nie, Z. D.; Fan, M.; Zhao, T. Y.; Cheng, Q. F.; Liu, M. J. Large-area ultrastrong and stiff layered MXene nanocomposites by shear-flow-induced alignment of nanosheets. *ACS Nano* **2022**, *16*, 12013–12023.

[37] Yin, Y.; Hu, K. S.; Grant, A. M.; Zhang, Y. H.; Tsukruk, V. V. Biopolymeric nanocomposites with enhanced interphases. *Langmuir* **2015**, *31*, 10859–10870.

[38] Zhang, Y. Y.; Gong, S. S.; Zhang, Q.; Ming, P.; Wan, S. J.; Peng, J. S.; Jiang, L.; Cheng, Q. F. Graphene-based artificial nacre nanocomposites. *Chem. Soc. Rev.* **2016**, *45*, 2378–2395.

[39] Ling, S. J.; Wang, Q.; Zhang, D.; Zhang, Y. Y.; Mu, X.; Kaplan, D. L.; Buehler, M. J. Integration of stiff graphene and tough silk for the design and fabrication of versatile electronic materials. *Adv. Funct. Mater.* **2018**, *28*, 1705291.

[40] Hu, K. S.; Gupta, M. K.; Kulkarni, D. D.; Tsukruk, V. V. Ultra-robust graphene oxide-silk fibroin nanocomposite membranes. *Adv. Mater.* **2013**, *25*, 2301–2307.

[41] Niu, Q. Q.; Huang, L.; Lv, S. S.; Shao, H. L.; Fan, S. N.; Zhang, Y. P. Pulse-driven bio-triboelectric nanogenerator based on silk nanoribbons. *Nano Energy* **2020**, *74*, 104837.

[42] Cheng, B. C.; Lei, Z. Y.; Wu, P. Y. Bio-derived crystalline silk nanosheets for versatile macroscopic assemblies. *Nano Res.* **2022**, *15*, 5538–5544.

[43] Drummy, L. F.; Farmer, B. L.; Naik, R. R. Correlation of the β-sheet crystal size in silk fibers with the protein amino acid sequence. *Soft Matter* **2007**, *3*, 877–882.

[44] Wongpinyochit, T.; Johnston, B. F.; Seib, F. P. Degradation behavior of silk nanoparticles-enzyme responsiveness. *ACS Biomater. Sci. Eng.* **2018**, *4*, 942–951.

[45] Wang, Y. Z.; Rudym, D. D.; Walsh, A.; Abrahamsen, L.; Kim, H. J.; Kim, H. S.; Kirker-Head, C.; Kaplan, D. L. *In vivo* degradation of three-dimensional silk fibroin scaffolds. *Biomaterials* **2008**, *29*, 3415–3428.